

Thermal stability of epitaxial cubic-TiN/ (Al,Sc)N metal/semiconductor superlattices

Jeremy L. Schroeder, Bivas Saha, Magnus Garbrecht, Norbert Schell, Timothy D. Sands & Jens Birch

Journal of Materials Science

Full Set - Includes 'Journal of Materials
Science Letters'

ISSN 0022-2461

J Mater Sci

DOI 10.1007/s10853-015-8884-5



Your article is protected by copyright and all rights are held exclusively by Springer Science +Business Media New York. This e-offprint is for personal use only and shall not be self-archived in electronic repositories. If you wish to self-archive your article, please use the accepted manuscript version for posting on your own website. You may further deposit the accepted manuscript version in any repository, provided it is only made publicly available 12 months after official publication or later and provided acknowledgement is given to the original source of publication and a link is inserted to the published article on Springer's website. The link must be accompanied by the following text: "The final publication is available at link.springer.com".

Thermal stability of epitaxial cubic-TiN/(Al,Sc)N metal/semiconductor superlattices

Jeremy L. Schroeder · Bivas Saha ·
Magnus Garbrecht · Norbert Schell ·
Timothy D. Sands · Jens Birch

Received: 28 October 2014 / Accepted: 30 January 2015
© Springer Science+Business Media New York 2015

Abstract We report on the thermal stability of epitaxial cubic-TiN/(Al,Sc)N metal/semiconductor superlattices with the rocksalt crystal structure for potential plasmonic, thermoelectric, and hard coating applications. TiN/Al_{0.72}Sc_{0.28}N superlattices were annealed at 950 and 1050 °C for 4, 24, and 120 h, and the thermal stability was characterized by high-energy synchrotron-radiation-based 2D X-ray diffraction, high-resolution (scanning) transmission electron microscopy [HR(S)/TEM], and energy dispersive X-ray spectroscopy (EDX) mapping. The TiN/Al_{0.72}Sc_{0.28}N superlattices were nominally stable for up to 4 h at both 950 and 1050 °C. Further annealing treatments for 24 and 120 h at 950 °C led to severe interdiffusion between the layers and the metastable cubic-Al_{0.72}Sc_{0.28}N layers partially transformed into Al-deficient cubic-(Al,Sc)N and the thermodynamically stable hexagonal wurtzite phase with a nominal composition of AlN (h-AlN). The h-AlN grains displayed two epitaxial variants with respect to c-TiN and cubic-(Al,Sc)N. EDX mapping

suggests that scandium has a higher tendency for diffusion in TiN/(Al,Sc)N than titanium or aluminum. Our results indicate that the kinetics of interdiffusion and the cubic-to-hexagonal phase transformation place constraints on the design and implementation of TiN/(Al,Sc)N superlattices for high-temperature applications.

Introduction

For 30 years, researchers have been pursuing epitaxial metal/semiconductor superlattices with low defect and dislocation densities for electronic, photonic, and plasmonic devices [1]. Saha et al. recently demonstrated epitaxial metal/semiconductor superlattices (i.e., TiN/Al_{0.72}Sc_{0.28}N) with low defect density [2]. The Al_{0.72}Sc_{0.28}N composition is lattice matched to TiN and scandium alloying increases the critical thickness of the metastable c-AlN layers [3]

J. L. Schroeder (✉) · M. Garbrecht · J. Birch
Thin Film Physics Division, Department of Physics, Chemistry,
and Biology (IFM), Linköping University, 581 83 Linköping,
Sweden
e-mail: jersc@ifm.liu.se

M. Garbrecht
e-mail: magnus.garbrecht@liu.se

J. Birch
e-mail: jebir@ifm.liu.se

B. Saha
School of Materials Engineering, Purdue University,
West Lafayette, IN 47907, USA
e-mail: bsaha@berkeley.edu

B. Saha
Birck Nanotechnology Center, Purdue University,
West Lafayette, IN 47907, USA

N. Schell
Helmholtz-Zentrum Geesthacht, Centre for Materials and
Coastal Research, Institute for Materials Research, Max-Planck-
Straße 1, 21502 Geesthacht, Germany
e-mail: norbert.schell@hzg.de

T. D. Sands
Bradley Department of Electrical and Computer Engineering and
Department of Materials Science and Engineering, Virginia
Tech, Blacksburg, VA 24061, USA
e-mail: sands@vt.edu

from 2 to 200 nm [2]. These metal/semiconductor superlattices show potential for applications as plasmonic metamaterials [4], high-temperature thermoelectric/thermionic devices, and hard coatings for cutting tools [5]. All three of these application areas require high-temperature thermal stability of the superlattice structure. Plasmonic applications depend on thermal stability due to localized heating [6]; nitride superlattices have been investigated for high-temperature thermoelectric applications up to 1000 °C [7, 8]; and (Ti,Al)N-based hard coatings for cutting tools routinely experience 700–1000 °C operating temperatures [9, 10].

Thus, we evaluated the high temperature behavior of TiN/Al_{0.72}Sc_{0.28}N superlattices via annealing experiments and ex situ characterization of the crystallographic and microstructural properties. The main results of this work are highlighted here:

- Metastable cubic-Al_{0.72}Sc_{0.28}N partially phase transforms into Al-deficient cubic-(Al,Sc)N and epitaxial h-AlN grains with increased annealing time.
- TiN and (Al,Sc)N layers of the superlattice interdiffuse with increased annealing time.
- Coherent nanometer-scale h-AlN grains are distributed throughout the film thickness due to layer intermixing.

Experimental

10/10 nm TiN/Al_{0.72}Sc_{0.28}N superlattices with the rocksalt crystal structure were deposited on (001)-oriented MgO substrates at 750 °C in a 10 mTorr Ar/N₂ (4 sccm Ar:6 sccm N₂) ambient via reactive dc-magnetron sputtering (PVD Products, Inc.) from scandium (99.998 % purity), aluminum (99.99 %), and titanium (99.99 %) targets (50 mm diameter × 6 mm thick) in a top-down confocal arrangement. The base pressure was 6.7×10^{-6} Pa (5.0×10^{-8} Torr) prior to deposition at 750 °C. Sputtering was performed in constant power mode (Al = 200 W; Sc = 180 W; Ti = 200 W) with a target to substrate distance of 9 cm and a substrate rotation speed of 5 rpm. Superlattices were deposited by opening and closing target shutters for the alternating TiN and Al_{0.72}Sc_{0.28}N layers.

Annealing treatments were performed in a custom-designed vacuum chamber annealing furnace using a Boralex tube heater. The vacuum chamber was evacuated to 6.7×10^{-4} Pa (5×10^{-6} Torr) before continuously flowing 30 sccm forming gas (5 % H₂:95 % N₂) to achieve a pressure of 8 mTorr. The superlattices were annealed (ramp rate = 20 °C min⁻¹) at 950 °C for 4, 24, and 120 h as well as 1050 °C for 4 and 24 h. All annealed superlattices originated from the same deposition. Furnace and sample temperatures were confirmed with a dual wavelength pyrometer (CellaTemp PA40; 0.95 and 1.05 μm).

The thermal stability of the 10/10 nm TiN/Al_{0.72}Sc_{0.28}N superlattices was characterized by annealing treatments followed by synchrotron-radiation-based X-ray diffraction imaging, high-resolution (scanning)/transmission electron microscopy (HR(S)/TEM), and energy dispersive X-ray spectroscopy (EDX) mapping. Synchrotron-radiation-based X-ray diffraction imaging was conducted at the High Energy Materials Science beamline P07 at PETRA III, DESY (Hamburg, Germany). Figure 1e provides a schematic of the X-ray diffraction setup. X-ray diffraction was conducted in transmission mode by directing a 10 μm × 400 μm X-ray beam approximately parallel to the film surface of a 4 × 4 × 0.5 mm³ sample, whereby diffraction occurs throughout the illuminated superlattice volume. The beam was approximately parallel to MgO [010], and the MgO substrate was partially irradiated by the X-ray beam, but no diffraction was observed from the MgO due to intentional misalignment of the MgO with respect to the X-ray beam. The 87.1 keV high-energy X-rays resulted in small diffraction angles (2°–10°), and the diffraction intensity was measured with a stationary Perkin Elmer XRD1621 2D detector placed 2500 mm from the sample, with the resulting 2D diffraction pattern representing a slice of reciprocal space.

HR(S)/TEM and EDX mapping were obtained using the Linköping probe- and image aberration-corrected and monochromated FEI Titan³ 60–300 microscope equipped with a high brightness XFEG source and ChemiSTEM Super-X detectors. The microscope was operated at an accelerating voltage of 300 kV. All TEM images were recorded with the beam parallel to MgO [010].

Results and discussion

Synchrotron-radiation-based X-ray diffraction imaging

Figure 1a–d presents 2D X-ray diffraction patterns for the as-deposited TiN/Al_{0.72}Sc_{0.28}N superlattice in addition to superlattices annealed at 950 °C for 4, 24, and 120 h. The as-deposited superlattice on a (001)-oriented MgO substrate is predominantly (002)-oriented as evidenced by the dominant 002 reflection (d-spacing = 2.13 Å), which is oriented along the growth direction (Fig. 1a). Corresponding diffraction peaks from the {002} family of planes are observed along the perimeter of the 002-diffraction ring. The 220 reflections originate from the same grains that produce the 002 reflections, with the location of the 220 reflections being determined by the 45° interplanar angle between the {220} and {002} planes in the cubic crystal system. Diffraction resulting from the periodicity of the superlattice is present in the form of superlattice reflections immediately below the 002 reflection from the

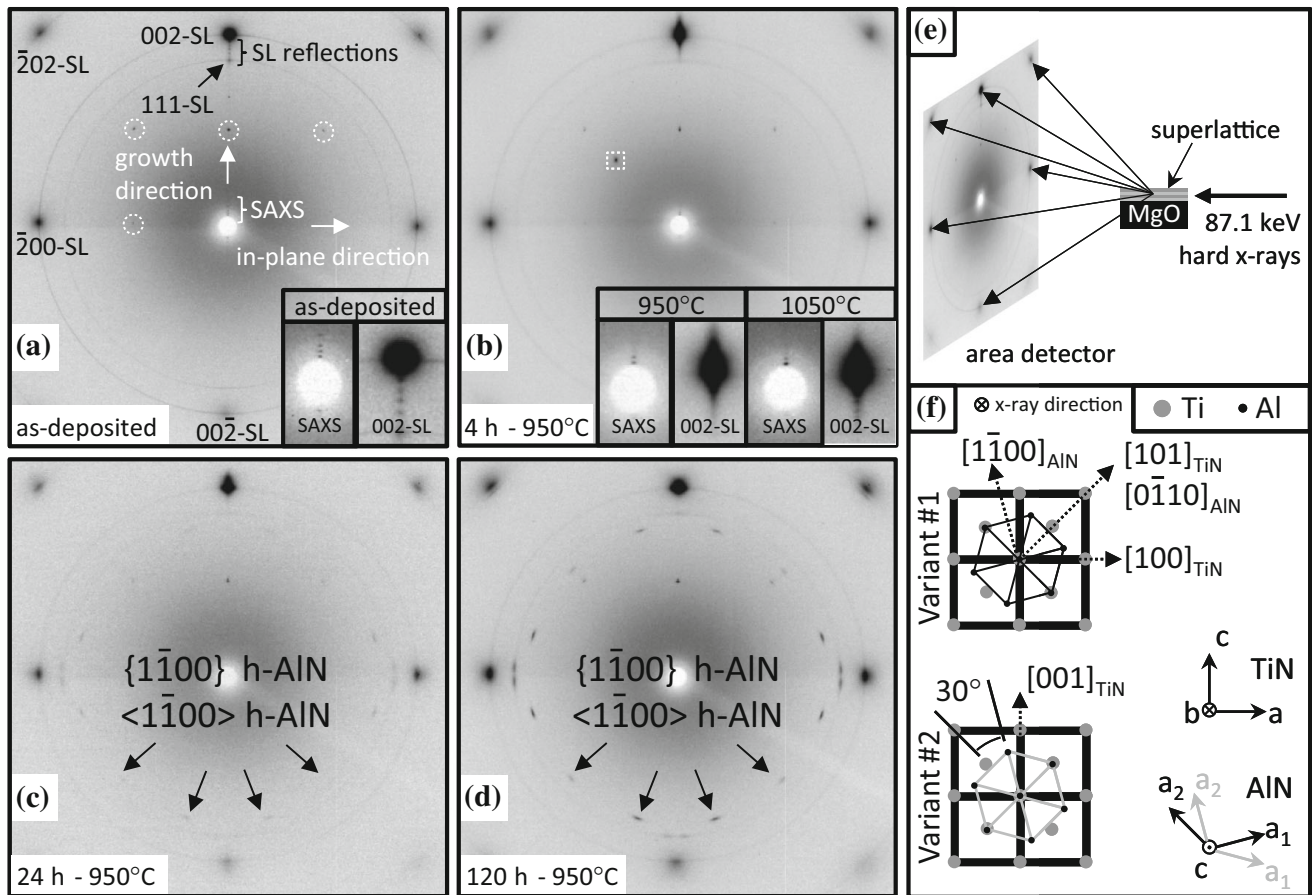


Fig. 1 **a** as-deposited superlattice is (002)-oriented and displays superlattice reflections and interference fringes in the SAXS signal; **b** superlattice reflections are still present after annealing for 4 h at both 950 and 1050 °C; **c** superlattice reflections have disappeared, and c-Al_{0.72}Sc_{0.28}N has begun to transform into Al-deficient (Al,Sc)N and h-AlN phases as indicated by 12 diffraction spots from two

variants of h-AlN; **d** increased annealing time leads to an increased concentration of h-AlN as indicated by darker h-AlN spots; **e** schematic of synchrotron-radiation-based 2D X-ray diffraction imaging of thin films in transmission mode; **f** schematic of two epitaxial variants (offset by 30°) of h-AlN on c-TiN

superlattice and interference fringes in the small angle X-ray scattering (SAXS) signal.

Standard lab-based X-ray diffraction (not shown) indicates that the as-deposited superlattices are epitaxial with strong (002)-texture. However, the full, but weak, 002- and 111-diffraction rings in the synchrotron-radiation diffraction patterns indicate that randomly oriented grains are also present in the microstructure, albeit a small fraction based on the low relative intensity of the diffraction rings compared to the 002 reflection from the superlattice. The presence of a weak superlattice 111 reflection (d-spacing = 2.46 Å) indicates some (111)-texture. The (111)-oriented grains are presumed to originate from the initial stages of film growth and are subsequently overwhelmed by the dominant (002)-oriented grains.

Other noteworthy features in the 2D X-ray diffraction patterns are as follows: first, the single-crystal MgO substrate does not produce any appreciable diffraction signal

since it is not exactly aligned with respect to the X-ray beam; second, the small diffraction spots highlighted with dashed circles are a duplicate representation of the main diffraction signal due to higher undulator X-ray beam harmonics and thus can be ignored; and third, the central white spot is due to a lead beam stop which protects the detector from the high-intensity non-diffracted direct X-ray beam.

The superlattice maintains most of its diffraction features, and no new additional phases are present after a 4 h anneal at 950 °C (Fig. 1b) indicating that the superlattices are nominally stable in the cubic rocksalt phase for at least 4 h at 950 °C. The inset images of Fig. 1b show close-up views of the data representing the SAXS-signal and 002 reflection from the superlattice (i.e., “002-SL”) at both 950 and 1050 °C. The decreasing intensity of the superlattice reflections compared to the as-deposited sample (inset images of Fig. 1a) indicates a gradual loss of

abruptness in the superlattice interfaces, which is explained by interdiffusion of the individual TiN and (Al,Sc)N layers, as discussed later.

We note an unidentified high-intensity diffraction spot (highlighted by a dashed square) in Fig. 1b. The spot corresponds to a d-spacing of 4.20 Å and is almost 45° from the surface normal. The d-spacing is closely related to the d-spacing of the 002 MgAl₂O₄ spinel planes, but we rule out the spinel structure due to the off-axis orientation, the peak not appearing at longer annealing times, and an EDX line profile analysis across the MgO/film interface showing no aluminum in the MgO substrate.

Figure 1c shows the superlattice after a 24 h anneal at 950 °C, with three new features of interest. First, the superlattice reflections have disappeared indicating that the film has lost its periodicity. Second, the onset of twelve equally spaced AlN {1 $\bar{1}$ 00} diffraction spots (d-spacing = 2.69 Å) indicates the formation of hexagonal-AlN that results from the cubic-Al_{0.72}Sc_{0.28}N phase losing aluminum. Höglund et al. observed similar behavior when annealing c-(Al,Sc)N thin films [11]. The twelve diffraction spots, which are 30° apart, are due to the presence of two different h-AlN grain orientations rotated 30° with respect to each other [12]. Figure 1f schematically presents the two h-AlN variants. The epitaxial relationship between h-AlN and c-TiN is (0001)[0 $\bar{1}$ 10] AlN// (001)[101] TiN. The twelve diffraction spots originate from horizontally oriented h-AlN grains, which are defined as h-AlN grains whose basal planes are perpendicular to the substrate surface. Vertically oriented h-AlN grains (i.e., basal planes parallel to the substrate surface) are also present, but their AlN {1 $\bar{1}$ 00} planes do not fulfill the diffraction condition. Third, peaks have appeared along the perimeter of the 111-diffraction ring. These peaks are caused by the h-AlN (0002) d-spacing (2.49 Å), which nearly coincides with the superlattice (111) d-spacing (2.46 Å). The location of these peaks implies that the h-AlN basal planes are tilted approximately 2.5° with respect to the TiN lattice. Both Chen et al. and Deng et al. have observed similar tilting behavior of h-AlN on TiN [13, 14]. The cubic-(Al,Sc)N phase continues to lose aluminum with extended annealing time as evidenced by the more prominent hexagonal-AlN diffraction spots after a 120 h anneal at 950 °C (Fig. 1d). Vertically oriented h-AlN grains (i.e., basal planes parallel to the substrate surface) are indicated by the two faint 0002 h-AlN reflections (d-spacing = 2.49 Å) at the bottom of the image.

HR(S)/TEM and EDX mapping

The STEM and EDX data of Fig. 2 clearly demonstrate increased intermixing of the TiN and (Al,Sc)N layers with

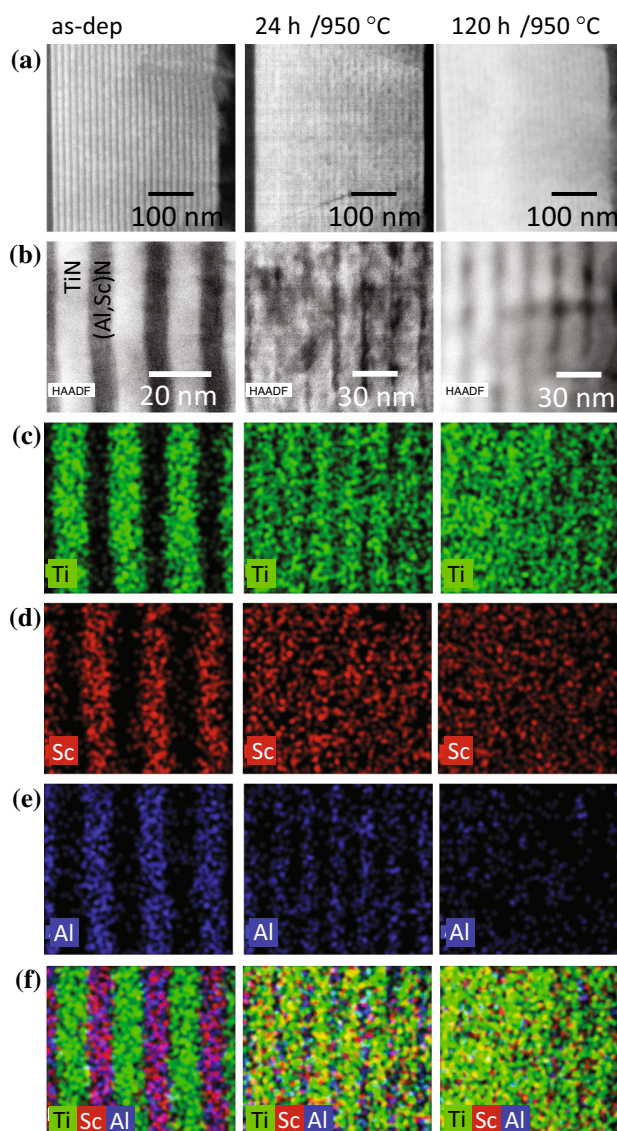


Fig. 2 (color online) Layer intermixing and loss of superlattice structure with increased annealing time confirmed with **a,b** (HAADF)-STEM micrographs; **c–e** EDX maps of titanium (Ti), scandium (Sc), and aluminum (Al); **f** combined elemental EDX maps

increased annealing time. Figure 2a, b displays high-angle annular dark field (HAADF)-STEM micrographs of the as-deposited superlattice as well as superlattices annealed for 24 and 120 h at 950 °C. Individual EDX maps of titanium, scandium, and aluminum from the same area as Fig. 2b are provided below each micrograph (Fig. 2c–e) in addition to combined EDX maps from titanium, scandium, and aluminum (Fig. 2f).

The (HAADF)-STEM micrograph of the as-deposited superlattice (Fig. 2b) shows distinct TiN layers (white) and (Al,Sc)N layers (gray) due to the atomic number dependence of the contrast mechanism in HAADF (Z-contrast). The corresponding EDX maps indicate that titanium is only

located in the TiN layers, while scandium and aluminum are only located in the (Al,Sc)N layers. After a 24 h anneal at 950 °C, the individual layers and interfaces are less distinct than the as-deposited state. The EDX maps show the onset of layer intermixing as a result of diffusion. The titanium and aluminum maps show diffuse layering compared to the as-deposited film, indicating titanium diffusion into the (Al,Sc)N layers and aluminum diffusion into the TiN layers, respectively. On the other hand, scandium appears to diffuse quite rapidly as indicated by a mostly uniform distribution of scandium. Activation energy data for metal diffusion in nitrides is limited [15], but our EDX results indicate that scandium has a higher tendency for diffusion in the TiN/(Al,Sc)N superlattice than titanium and aluminum. The superlattice annealed for 120 h at 950 °C shows a uniform distribution of all three elements (Ti, Sc, and Al), indicating that a significant amount of intermixing has occurred. It is also worthwhile to note that the aluminum concentration visualized in Fig. 2e is decreasing with increased annealing time, a trend that was confirmed by EDX analysis (as-deposited = 20 ± 2 %; 120 h/950 °C = 8 ± 2 %). The loss of aluminum is likely due to surface evaporation after aluminum is released from the nitride lattice and diffuses to the surface. Released aluminum could also diffuse to the MgO substrate and react with the MgO to form a spinel structure, but our analysis indicates that there is no detectable spinel formation.

Both Setoyama et al. [16] and Kim et al. [17] report that TiN/AlN superlattices exhibit good thermal stability, but their annealing treatments were limited to less than

3.5 h at 1000 °C. Our 4 h annealing results agree with both of these reports, whereas our extended annealing treatments show significant interdiffusion. Intermixing of nitride superlattices at elevated temperature has also been observed in TiN/CrN [18], TiAlN/CrN [19], TiN/NbN [15], and ZrN/ScN [20] multilayer systems.

Figure 3 shows cross-sectional HRTEM micrographs of the as-deposited and 120 h/950 °C annealed superlattices. The as-deposited superlattice (Fig. 3a) shows distinct layers with coherent interfaces, and the Fourier Transform (FT) verifies a cubic crystal structure (inset image). The d-spacing of the first diffraction spots (i.e., 2.11 Å) in the FT corresponds to the cubic phase of (Al,Sc)N, where $d_{200}(\text{c-AlN}) = 2.02$ Å and $d_{200}(\text{c-ScN}) = 2.22$ Å. On the other hand, the superlattice layers are no longer visible after annealing for 120 h at 950 °C (Fig. 3b), and the FT verifies the presence of both cubic and hexagonal grains (inset image) due to the original cubic- $\text{Al}_{0.72}\text{Sc}_{0.28}\text{N}$ phase losing aluminum and forming the hexagonal-AlN phase. Due to layer interdiffusion, the h-AlN grains are distributed randomly throughout the film instead of being concentrated at the original location of the (Al,Sc)N layers. The d-spacing of the 002 cubic-(Al,Sc)N reflection increased due to loss of aluminum.

The HRTEM micrograph (Fig. 4a) shows the presence of a cubic matrix with two h-AlN grains of different variants. The cubic and hexagonal crystal structures are confirmed in Fig. 4c, which is the FT of Fig. 4a, and the diffraction spots are visually highlighted in Fig. 4d. As expected, the orientational relationship of the h-AlN diffraction spots with respect to the cubic lattice observed

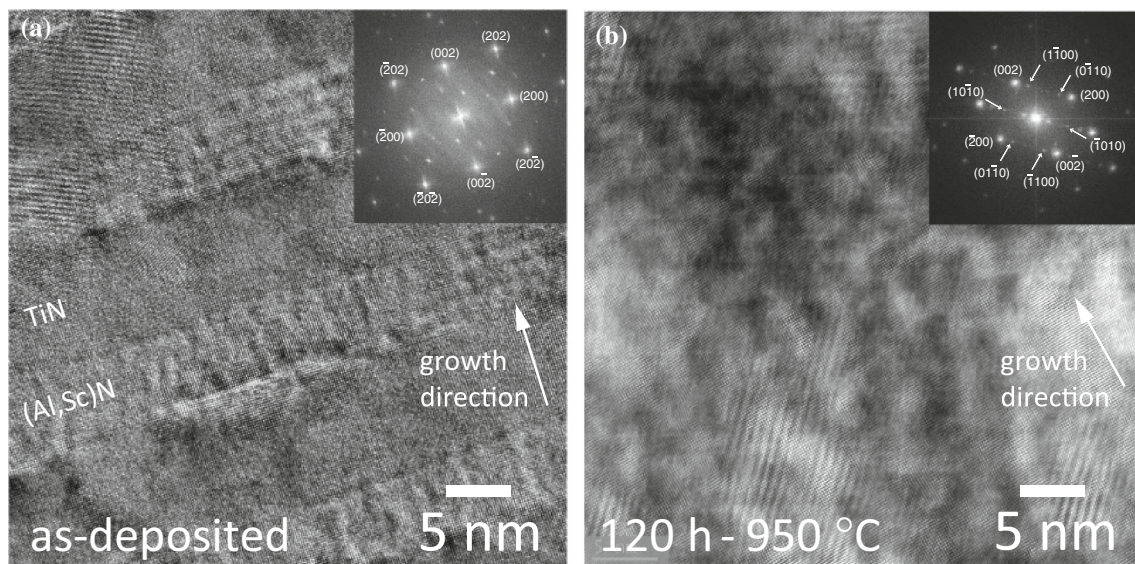


Fig. 3 HRTEM micrograph of **a** as-deposited superlattice shows distinct layers with coherent interfaces (inset Fourier Transform (FT) shows cubic structure); **b** 120 h/950 °C annealed superlattice shows

significant intermixing and Moiré fringes (inset FT indicates the presence of cubic and hexagonal grains)

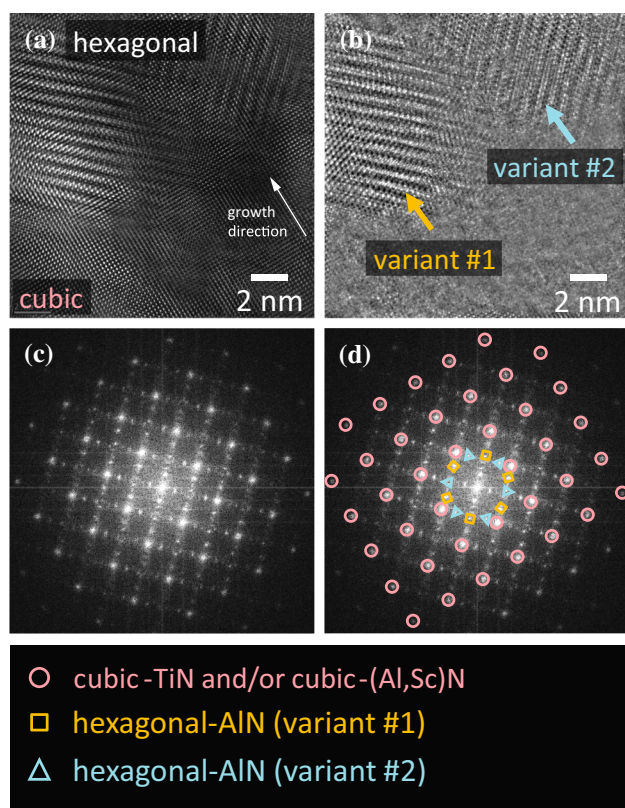


Fig. 4 (color online) **a** HRTEM micrograph of a superlattice annealed for 120 h at 950 °C. Hexagonal-AlN grains are present within a c-TiN and Al-deficient (Al,Sc)N matrix. **b** Inverse Fourier Transform of **a** while masking the cubic diffraction spots shows the location of hexagonal grains. **c** Fourier Transform of **a** shows diffraction from the cubic matrix and the two epitaxial variants of h-AlN. **d**, **c** overlaid with identification markers (legend at bottom). The Moiré patterns contribute to the intensity found in between the main lattice reflections

in the FT is identical to the orientation relationship observed in the 2D X-ray diffraction pattern of Fig. 1d. The locations of the h-AlN grains are clearly identified in Fig. 4b, which is an inverse FT of Fig. 4a while masking the cubic diffraction spots. The inverse FT shows the location of the contrast motif contributing to the hexagonal spot pattern.

Conclusion

TiN/Al_{0.72}Sc_{0.28}N superlattices exhibit limited thermal stability at 950 °C due to interdiffusion and the phase transformation of metastable cubic Al_{0.72}Sc_{0.28}N. The superlattice structure is maintained after a 4-h annealing treatment at 950 °C, but severe interdiffusion of the superlattice layers and the transformation of metastable cubic-Al_{0.72}Sc_{0.28}N to Al-deficient (Al,Sc)N and h-AlN occur during a 24-h annealing treatment at 950 °C. The h-AlN

grains are randomly distributed throughout the film due to layer interdiffusion. The application space and maximum operating temperature for TiN/(Al,Sc)N superlattices are thus limited by the kinetics of interdiffusion and the phase transformation. TiN/(Al,Sc)N superlattices may be a viable material for high-temperature applications with short lifetimes (minutes/hours), such as hard coatings in cutting tools, but applications with long lifetimes (months/years), such as thermoelectrics, will require reduced operating temperatures to avoid interdiffusion and phase transformation.

Acknowledgements J. L. Schroeder and J. Birch acknowledge financial support from Linköping University and the Swedish Research Council (the RÅC Frame Program (2011-6505) and the Linnaeus Grant (LiLi-NFM)). B. Saha and T. D. Sands acknowledge financial support by the National Science Foundation and US Department of Energy (CBET-1048616). The Knut and Alice Wallenberg (KAW) Foundation is acknowledged for the Electron Microscope Laboratory in Linköping. Special thanks to Lina Rogström, Niklas Norrby, and Daniel Ostach for assistance with the synchrotron-radiation measurements.

References

- Sands T, Palmström CJ, Harbison JP, Keramidias VG, Tabatabaie N, Cheeks TL, Silberberg Y (1990) Stable and epitaxial Metal/III-V semiconductor heterostructures. *Mater Sci Rep* 5:98–170
- Saha B, Saber S, Naik GV, Boltasseva A, Stach EA, Kvam EP, Sands TD (2014) Development of epitaxial Al_xSc_{1-x}N for artificially structured metal/semiconductor superlattice metamaterials. *Phys Status Solidi B*. doi:10.1002/pssb.201451314
- Wong MS, Hsiao GY, Yang SY (2000) Preparation and characterization of AlN/ZrN and AlN/TiN nanolaminate coatings. *Surf Coat Technol* 133:160–165
- Naik GV, Saha B, Liu J, Saber SM, Stach EA, Irudayaraj JMK, Sands TD, Shalaev VM, Boltasseva A (2014) Epitaxial superlattices with titanium nitride as a plasmonic component for optical hyperbolic metamaterials. *Proc Natl Acad Sci USA* 111:7546–7551
- Saha B, Lawrence SK, Schroeder JL, Birch J, Bahr DF, Sands TD (2014) Enhanced hardness in epitaxial TiAlScN alloy thin films and rocksalt TiN/(Al, Sc)N superlattices. *Appl Phys Lett* 105:151904
- Guler U, Boltasseva A, Shalaev VM (2014) Refractory plasmonics. *Science* 344:263–264
- Zebarjadi M, Bian ZX, Singh R, Shakouri A, Wortman R, Rawat V, Sands T (2009) Thermoelectric transport in a ZrN/ScN superlattice. *J Electron Mater* 38:960–963
- Shakouri A, Zebarjadi M (2009) Nanoengineered materials for thermoelectric energy conversion. In: Volz S (ed) *Thermal nanosystems and nanomaterials*. Springer, Berlin, pp 225–299
- Norrby N, Johansson MP, M'saoubi R, Oden M (2012) Pressure and temperature effects on the decomposition of arc evaporated Ti_{0.6}Al_{0.4}N coatings in continuous turning. *Surf Coat Technol* 209:203–207
- Carvalho SR, Silva S, Machado AR, Guimaraes G (2006) Temperature determination at the chip-tool interface using an inverse thermal model considering the tool and tool holder. *J Mater Process Technol* 179:97–104
- Hoglund C, Alling B, Birch J, Beckers M, Persson POA, Baetz C, Czizany Z, Jensen J, Hultman L (2010) Effects of volume

- mismatch and electronic structure on the decomposition of ScAlN and TiAlN solid solutions. *Phys Rev B* 81:224101
12. Ghafoor N, Johnson LJS, Klenov DO, Demeulemeester J, Desjardins P, Petrov I, Hultman L, Oden M (2013) Nanolabyrinthine ZrAlN thin films by self-organization of interwoven single-crystal cubic and hexagonal phases. *APL Mat* 1:022105
 13. Chen D, Wang YM, Ma XL (2009) Size-effect on stress behavior of the AlN/TiN film. *Acta Mater* 57:2576–2582
 14. Deng RP, Murali P, Gall D (2012) Biaxial texture development in aluminum nitride layers during off-axis sputter deposition. *J Vac Sci Technol A* 30:051501
 15. Engstrom C, Birch J, Hultman L, Lavoie C, Cabral C, Jordan-Sweet JL, Carlsson JRA (1999) Interdiffusion studies of single crystal TiN/NbN superlattice thin films. *J Vac Sci Technol A* 17:2920–2927
 16. Setoyama M, Irie M, Ohara H, Tsujioka M, Takeda Y, Nomura T, Kitagawa N (1999) Thermal stability of TiN/AlN superlattices. *Thin Solid Films* 341:126–131
 17. Kim DG, Seong TY, Baik YJ (2002) Effects of annealing on the microstructures and mechanical properties of UN/AlN nanomultilayer films prepared by ion-beam assisted deposition. *Surf Coat Technol* 153:79–83
 18. Barshilia HC, Jain A, Rajam KS (2003) Structure, hardness and thermal stability of nanolayered TiN/CrN multilayer coatings. *Vacuum* 72:241–248
 19. Barshilia HC, Prakash MS, Jain A, Rajam KS (2005) Structure, hardness and thermal stability of TiAlN and nanolayered TiAlN/CrN multilayer films. *Vacuum* 77:169–179
 20. Burmistrova P (2012) Microstructure and thermoelectric properties of ScN thin films and metal/ScN superlattices for high-temperature energy conversion. Ph.D. Dissertation, Purdue University